JOURNAL OF SPACECRAFT AND ROCKETS
Vol. 34, No. 2, March–April 1997

Turbulent Flow Structure Characterization of Angled Injection into a Supersonic Crossflow

Rodney D. W. Bowersox*
U.S. Air Force Institute of Technology, Wright–Patterson Air Force Base, Ohio 45433-7755

An experimental analysis of the three-dimensional, turbulent, compressible flow structure of a highly underexpanded Mach 1.8 jet injected at an angle of 25 deg into a Mach 2.9 freestream is described. The experimental methods include cross-film anemometry, conventional mean-flow probes (pitot and cone-static pressure), schlieren photography, and surface oil-flow visualization. The mean-flow data consist of axial mass flux, *y*-*z* plane mass flux vector, and total pressure contour plots. Turbulence data include *x*, *y*, and *z* mass flux turbulence intensity components, *x*-*y* and *x*-*z* Reynolds shear stresses, and anisotropy coefficients. Two relatively large recirculation cells were located just downstream of the injector. In addition, the vortex pair within the plume dramatically affected the overall mean and turbulent flow structure. The axial turbulence intensity had two peaks that were collocated with the vortex pair. The transverse and spanwise intensities peaked on the right and left sides of the plume, respectively. The anisotropy contours also showed a strong dependence on the secondary motion of the two counter-rotating vortices. In particular, the *z*-*y* coefficient had a maximum located within one vortex, and a minimum in the other.

Nomenclature

A	= anisotropy coefficient
k	= turbulent kinetic energy
M	= Mach number
p	= pressure
Re	= Reynolds number
S_{ij}	= $(\partial\bar{u}_i/\partial x_j + \partial\bar{u}_i/\partial x_j)/2$
T	= temperature
u, v, w	= x, y, z velocity components
x, y, z	= Cartesian coordinates
δ	= boundary-layer thickness
λ	= bulk viscosity
μ	= molecular viscosity
Π	= $\tau_{ij}^L + \tau_{ij}^T$
ρ	= density
τ	= shear stress
τ_{ij}^L	= $\mu(u_{i,j} + u_{j,i}) + \lambda\delta_{ij}\nabla\cdot\bar{V}$
τ_{ij}^T	= Favre-averaged turbulent shear stress
Ω_{ij}	= $(\partial\bar{u}_i/\partial x_j - \partial\bar{u}_i/\partial x_j)/2$
$\bar{\omega}$	= $\nabla x\bar{V}$

Subscripts

c	= compressible, or cone-static pressure
e	= effective
j	= jet
o	= reference condition
t	= total condition
∞	= freestream condition
1	= local condition
2	= behind normal shock (pitot pressure)

Superscripts

L	= laminar
T	= turbulent
$'$	= Reynolds (time-averaged) fluctuating component
-	= Reynolds mean component

Received March 27, 1996; revision received July 24, 1996; accepted for publication Aug. 30, 1996.

*Assistant Professor, Aerospace Engineering, Department of Aeronautics and Astronautics, Graduate School of Engineering. Member AIAA.

Introduction

INJECTION into a supersonic crossflow is important for a number of practical applications; for example, thrust vector control, supersonic combustion ramjet fuel injection, and boundary-layer control. The overall structure of the mean flowfield associated with injection into a supersonic cross stream has been the subject of much investigation.[1–10] The earlier studies[2–4] concentrated on developing techniques to predict the plume and Mach disk trajectories. Those studies mainly used schlieren photography, pitot pressure probes, and concentration probes, for dissimilar gaseous injection, to quantify the mean flowfield. The effects of injection angle, including yaw, on the mean concentration field also have been investigated.[5–8] In addition, the upstream interaction has been the subject of study.[9]

As a result of the large number of studies, the mean-flow physics of supersonic injection into a supersonic crossflow are reasonably understood. First, the injection into a supersonic freestream creates what is usually termed the interaction shock, which generally separates the incoming boundary layer. Thus, the familiar lambda-shock/boundary-layer interaction structure is generated. Because of the unsteady nature of the shock/boundary-layer interaction, the interaction shock position is also unsteady. In the case in which the incoming boundary layer was laminar,[9] the separation region was relatively large. For turbulent boundary layers, as is the case for the present study, the separation region is usually much smaller. As the jet emerges, it is turned downstream by the incoming high-momentum freestream. Also, as the underexpanded jet emerges, it expands to conditions requiring termination at a normal shock called the Mach disk.[3] Directly behind the injector, the flow is separated, which is followed by a reattachment of the flow and a recompression shock. Again, on account of the unsteady separation regions, the recompression shock position is also unsteady. A relatively strong counter-rotating vortex pair is present within the plume. Most of the evidence for the vortex pair has been based upon the kidney-bean shape of the plume.[11] In addition, low-speed measurements have confirmed the existence of the vortex pair.[12–14] A smaller, weaker horseshoe vortex, similar to that generated by a wing-body junction, occurs at the injection–crossflow junction. It also has been documented that a vortex street results from the flow separation just downstream of the jet.[15] A fourth, near-field, exit ring-like vortex system also has been reported for low-speed flows.[15,16] This system is believed to be the result of the shedding of injector boundary-layer vorticity.

The turbulent flow structure associated with supersonic injection is more complex and significantly less understood than the mean flowfield. However, a number of low-speed studies have been performed.[12–16] Even though there are many similarities between

the high-speed and low-speed injection flows, significant differences also exist. For example, it has been well established that turbulent mixing is severely inhibited by compressibility.[17,18] Second, the upstream shock/boundary-layer interaction adds complications to the compressible-flow case. Compressibility also can affect the vorticity field via the baroclinic torque and bulk dilatation, which are both zero for incompressible flows. Because high-speed studies that include turbulence measurements[10,19] are rare, a substantial amount of the current understanding of these flows has been founded in reasonable extrapolations of the incompressible knowledge base.

Although computational fluid dynamics has become a very important research and design tool, the lack of computational resources necessary for direct numerical or large eddy simulation of practical high-Reynolds-number turbulent flows means that engineers must rely on an approximate averaged form of the governing Navier–Stokes equations. Mass-weighted-time or Favre averaging is adopted almost universally.[20] Hence, at present, simulation of injection flows is limited by the accuracy of the turbulence modeling methodology employed, and the development of models suitable for injection flows has been severely hindered by the extreme dearth of turbulence data.

The purpose of the present study is to provide insight into the three-dimensional turbulent flow structure associated with supersonic injection flow. Cross-film anemometry, along with conventional pitot and cone-static pressure probes, was incorporated to provide mass-weighted mean and turbulent flow information. In addition, flow visualization techniques (schlieren photography and surface oil flow) were used to provide qualitative insight into the overall structure of the flowfield. The mean-flow data presented here include contours of total pressure and mass flux. The turbulence measurements include contour plots of mass flux turbulence intensity, x-y and x-z plane turbulent Reynolds shear stresses, and anisotropy coefficients.

Experimental Apparatus

Facilities

All tests were performed in the U.S. Air Force Institute of Technology pressure-vacuum supersonic wind tunnel. The freestream Mach number across the nozzle exit plane for this facility is 2.9, with a ± 0.03 variation. The settling-chamber pressure and temperature were maintained at 2.0 ± 0.03 atm and 294 ± 2 K for all tests. The freestream Re/m was 15×10^6. The freestream turbulent kinetic energy was 0.016% of the freestream mean specific kinetic energy. The test section is $6.35 \times 6.35 \times 28.0$ cm.

The injector model was built into the ceiling of the tunnel as shown in Fig. 1; also shown is the coordinate system. The injectant gas was air at $M = 1.8$. The throat and exit diameters of the conical nozzle were 3.22 and 3.86 mm, respectively. The injector-nozzle divergence angle was 0.83 deg. The injection angle was 25 deg relative to the freestream. Because the injector was at an angle, the exit port was elliptical with 3.86 and 9.14 mm minor and major axis lengths, respectively. The injectant total pressure and temperature were 3.8 ± 0.03 atm and 294 ± 2 K, respectively. The injection parameters $P_{tj}/P_{t\infty}$, P_j/P_∞, u_j/u_∞, ρ_j/ρ_∞ were 1.93, 10.5, 0.79, and 6.47, respectively.

Data Analysis

Microsecond spark schlieren photographs of the flowfield were taken, and surface oil-flow visualizations were obtained. Conventional pitot (p_{t2}) and 10 ± 0.03 deg semivertex angle cone-static pressure (p_c) probe surveys were acquired. The ratio of these data allowed for the calculation of the local total pressure (p_{t1}) (Ref. 21). Normalized uncertainty estimates are summarized in Table 1. The uncertainty estimates account for the propagation of pitot and cone-static probe transducer calibration, probe location, and tunnel condition repeatability uncertainties through the data reduction analysis to arrive at the local total pressure.

TSI brand IFA 100 constant-temperature anemometer systems were used with cross-film sensors.[22] TSI 1243-20 and 1243-20AN cross-film probes were used. Each of the two platinum hot-film cylindrical sensors on a probe had a length of 1.0 mm and a diameter of 51 μm. The two sensors on a probe were nominally 1.0 mm apart. Cross-film measurements were obtained in both the x-y (1243-20 probes) and the x-z (1243-20AN probes) planes. The frequency response was optimized to nominally 150 kHz by the square-wave technique in the Mach 2.9 freestream. All of the present data were taken using the single overheat technique,[23] where the resistance ratio was set to 2.03 ± 0.03. In a related study, McCann and Bowersox[19] demonstrated that the single overheat technique was adequate for the present adiabatic flow. All probes were designed for boundary-layer type measurements. Hence, flow access for all data was through the tunnel floor.

The cross-film data reduction techniques used here were founded in the analyses of Kovasznay[24] and Spangenberg.[25] In general, the reduction was based on the empirical heat-loss formula

$$Nu = a\sqrt{Re_e} + b \tag{1}$$

Table 1 Uncertainty analysis results

Measurement	Error, %	Figure no.
$P_t/P_{t\infty}$	11.0	3
$\overline{\rho u_i}/(\rho u)_\infty$	6.0	4
$\sqrt{[(\rho u)'^2]}/\overline{\rho u}$	9.0	5
Anisotropy	18.0	6, 7
Shear stress	20.0	8

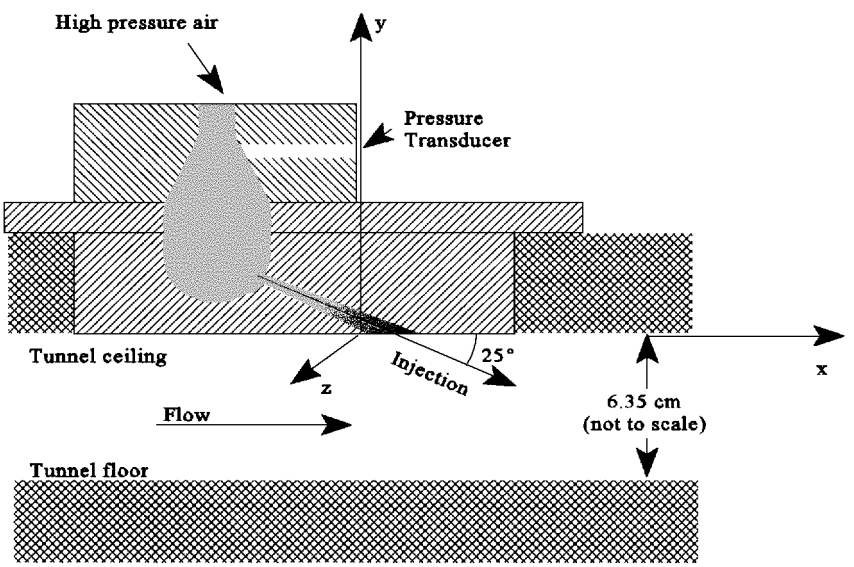

Fig. 1 Schematic of wind-tunnel model.

where Nu is the wire Nusselt number, and Re_e is the effective cooling Reynolds number.[23,26] On the basis of the findings of Spangenberg,[25] the cosine law was assumed valid. In addition, the flow angles in the present thin-layer type of flow did not deviate substantially from those of the calibration. In general, single overheat cross-wire anemometry provides the mean mass flux components, $\overline{\rho u_i}$, the mass flux turbulence intensities, $\sqrt{[(\rho u_i)'^2]}$, and the $\overline{(\rho u_i)'(\rho u_j)'}$ correlation.[23] The uncertainty estimates, accounting for the propagation of calibration, probe location, and tunnel condition repeatability uncertainties, are summarized in Table 1. McCann and Bowersox[19] confirmed that the Reynolds shear stress, including the compressibility terms, was directly measurable with the cross-film probe for the present flow.

The probes were calibrated by placing them in the tunnel freestream and varying the tunnel total pressure. Because a single data contour involved a series of tunnel runs, the probes were intermittently calibrated throughout the testing matrix to ensure that they had not suffered from oxidation or contamination. The minimum linear regression correlation coefficient for any of the calibrations was 0.995.

Anisotropy coefficients[26] provide insight into the structure of the turbulent flow by comparing the relative magnitudes of the turbulent fluctuation components. For the present study, three conventional anisotropy coefficients were calculated as

$$A_{xy} = \frac{\sqrt{\overline{(\rho v)'^2}}}{\sqrt{\overline{(\rho u)'^2}}}, \qquad A_{xz} = \frac{\sqrt{\overline{(\rho w)'^2}}}{\sqrt{\overline{(\rho u)'^2}}}, \qquad A_{zy} = \frac{\sqrt{\overline{(\rho v)'^2}}}{\sqrt{\overline{(\rho w)'^2}}} \tag{2}$$

A fourth, three-dimensional anisotropy parameter was defined here to represent overall magnitude of the fluctuating mass flux vector, i.e.,

$$A \equiv \frac{\sqrt{1 + A_{xy}^2 + A_{xz}^2}}{\sqrt{3}} \tag{3}$$

The three-dimensional parameter in Eq. (3) was normalized to the isotropic condition by the $\sqrt{3}$ factor in the denominator. Taken with Eq. (2), the three-dimensional anisotropy parameter provides a convenient manner in which to assess the level of isotropy of the turbulent flow. See Table 1 for the random-error estimates.

Results and Discussion

Flow Visualization

Presented in Fig. 2a is a schlieren photograph of the present flow. The flow was from left to right, and the injector was in the ceiling.

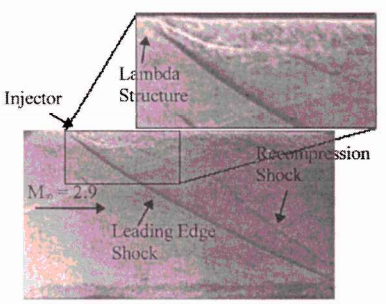

a) Schlieren

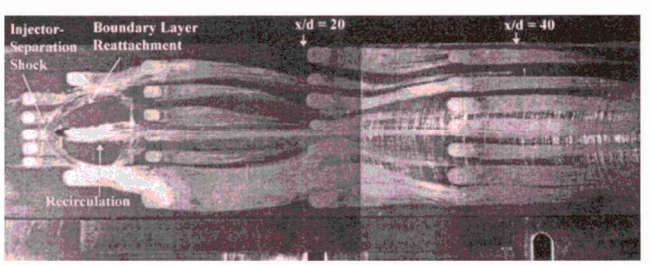

b) Surface oil flow

Fig. 2 Flow visualization.

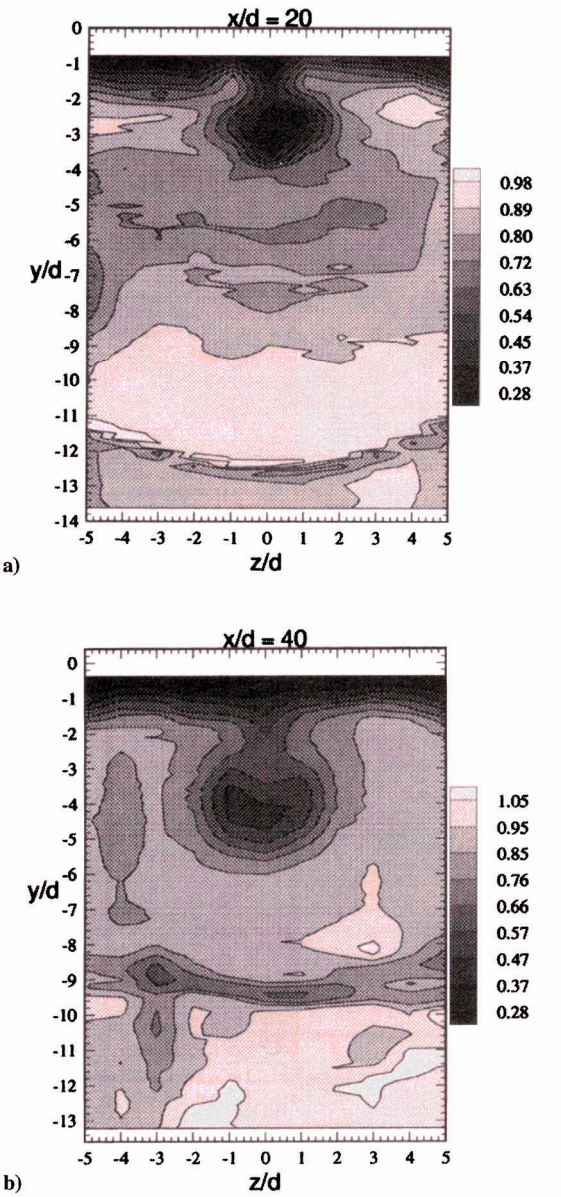

Fig. 3 Total pressure contours ($P_{t1}/P_{t\infty}$).

The salient flow features include the injector interaction shock, the injection plume, and a recompression shock just downstream of the injector. Recall from the Introduction that the position of the two shocks was expected to be somewhat unsteady. After comparing five photographs, it was noticed that at $x/d = 17$, the location of the interaction and recompression shock varied by roughly $0.1d$ (0.4 mm) and $0.3d$ (1.1 mm), respectively. The enlarged region near the injector shows a very small lambda-shock structure that is indicative of boundary-layer separation. The $x/d = 20$ measurement station also is annotated on Fig. 2a. At $x/d = 20$, the interaction shock was located at roughly $y/d = -12.5$, and the recompression shock was at $y/d \approx -8.0$. The facility boundary layers also are depicted in Fig. 2a. The boundary-layer/injection diameter ratio δ_∞/d was estimated to be 1.6.

The surface oil-flow visualization is shown in Fig. 2b. The initial oil-drop locations are clearly depicted on the figure. For this run, the injector was placed in the tunnel floor. The flow in Fig. 2b was from left to right. The vertex of a set of two curved lines that were symmetric about the x-y plane centerline (i.e., the flow or tunnel centerline) was located just upstream of the injector. The first line, progressing in a downstream fashion, was the result of the interaction shock separating the incoming boundary layer approximately 1.1 jet diameters upstream of the injector. The second line shows

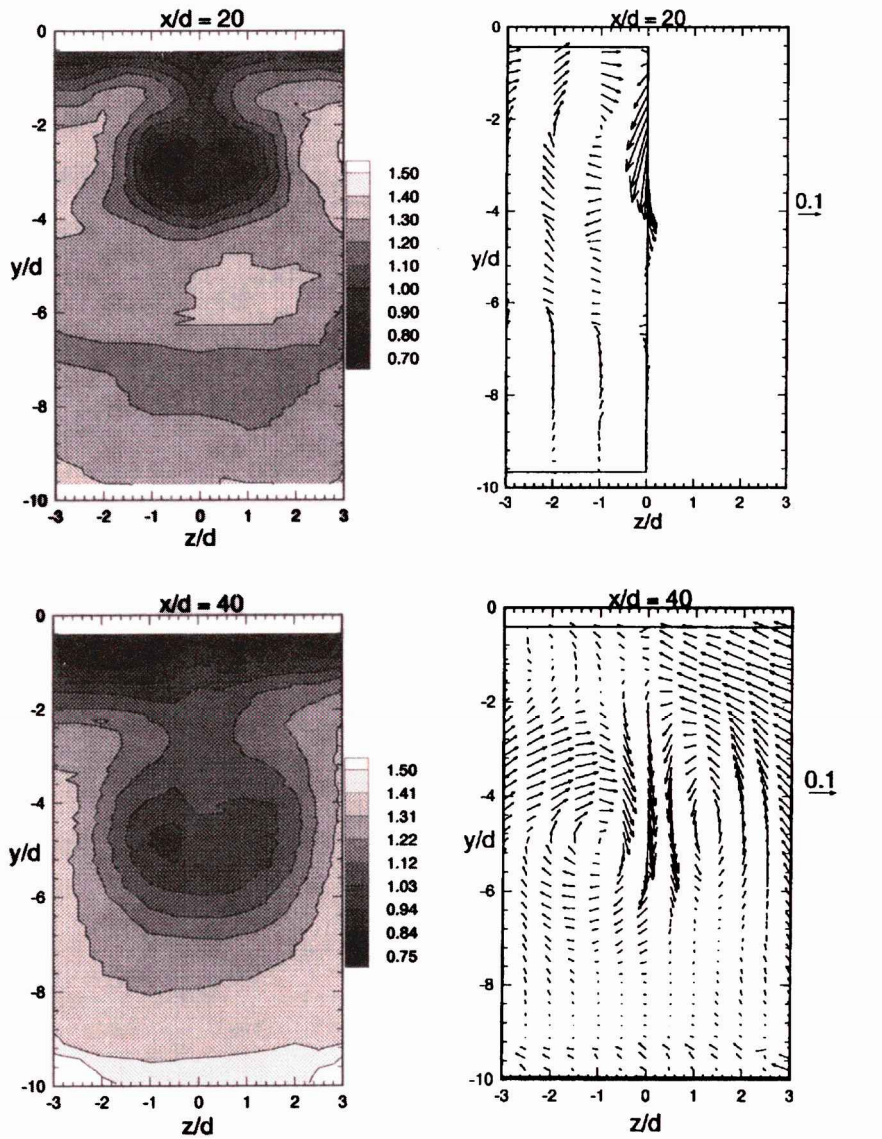

Fig. 4 Mean mass flux contours.

the reattachment location. As the oil progressed downstream and around the injector, it was primarily confined between the separation and reattachment lines. In addition, a significant amount of oil was drawn back upstream along the centerline x-y plane just behind the injector. Thus, two recirculation cells, which were symmetric about the injection centerline, were located just downstream of the injector. As indicated by the oil-flow pattern, the $x/d = 20$ station was located just upstream of the interaction-shock sidewall reflections crossing the plume. The second station was positioned well downstream of this crossing, where the shocks were again just striking the outer walls. Hence, they were completely out of the measurement region. The effects of the reflected shocks on the measured mean and turbulent flow properties are discussed in the following two sections.

Mean-Flow Results

Total pressure contour plots are given in Fig. 3. The contours were constructed from a series of y profiles. The conventional mean-flow profiles were acquired in $\Delta z/d$ increments of 1.0. The contour plots are oriented such that the flow is going into the page. The injection plume is depicted clearly in each plot. As mentioned in the Introduction, because of the main vortex pair, the cardioid-shaped nature of the injection core was expected.[13–15] If, for comparison, the plume center is assumed to be collocated with the maximum concentration for dissimilar gaseous injection, then the present penetration heights of $3.0d$ and $4.5d$ at $x/d = 20$ and 40, respectively, are in reasonable agreement with the overexpanded, 30-deg-angled, helium injection case (mass flux ratio of 2.16) of Mays et al.[6] The injection interaction shock is shown clearly near the bottom ($y/d \approx -12.5$) of the $x/d = 20$ contour. The effects of the recompression shock at $x/d = 20$ also are evident ($y/d \approx -7.5$). The $z/d = 0$ shock locations at $x/d = 20$ were in excellent agreement with measurements from Fig. 2a. In addition, the leading-edge interaction shock resulted in a freestream total pressure loss of about 4.0–6.0%. The measured shock angle in this region of the flow (see Fig. 2a) was roughly 30.0 deg. Using conical flow theory, a 4.2% loss was predicted. These results indicated that the shock was not very strong. Because a relatively low freestream total pressure loss occurred through the combined interaction shock and reflected shocks (total loss of roughly 10%) at $x/d = 40$, it was expected that the shock interacting with the plume had a minimal effect on the overall plume mean-flow structure.

Presented in Fig. 4a are the mean axial mass flux contours measured with the cross-film probes. For these data, the measurement field was reduced to just capture the plume, and the spatial resolution in the z direction was doubled, i.e., $\Delta z/d = 0.5$. The results in Fig. 4 show the same salient flow features as those described in the preceding paragraph, where again the effects of the shock interaction with the plume were unnoticeable. The y-z plane mass flux vector plots are given in Fig. 4b. Note that, because of probe attrition,

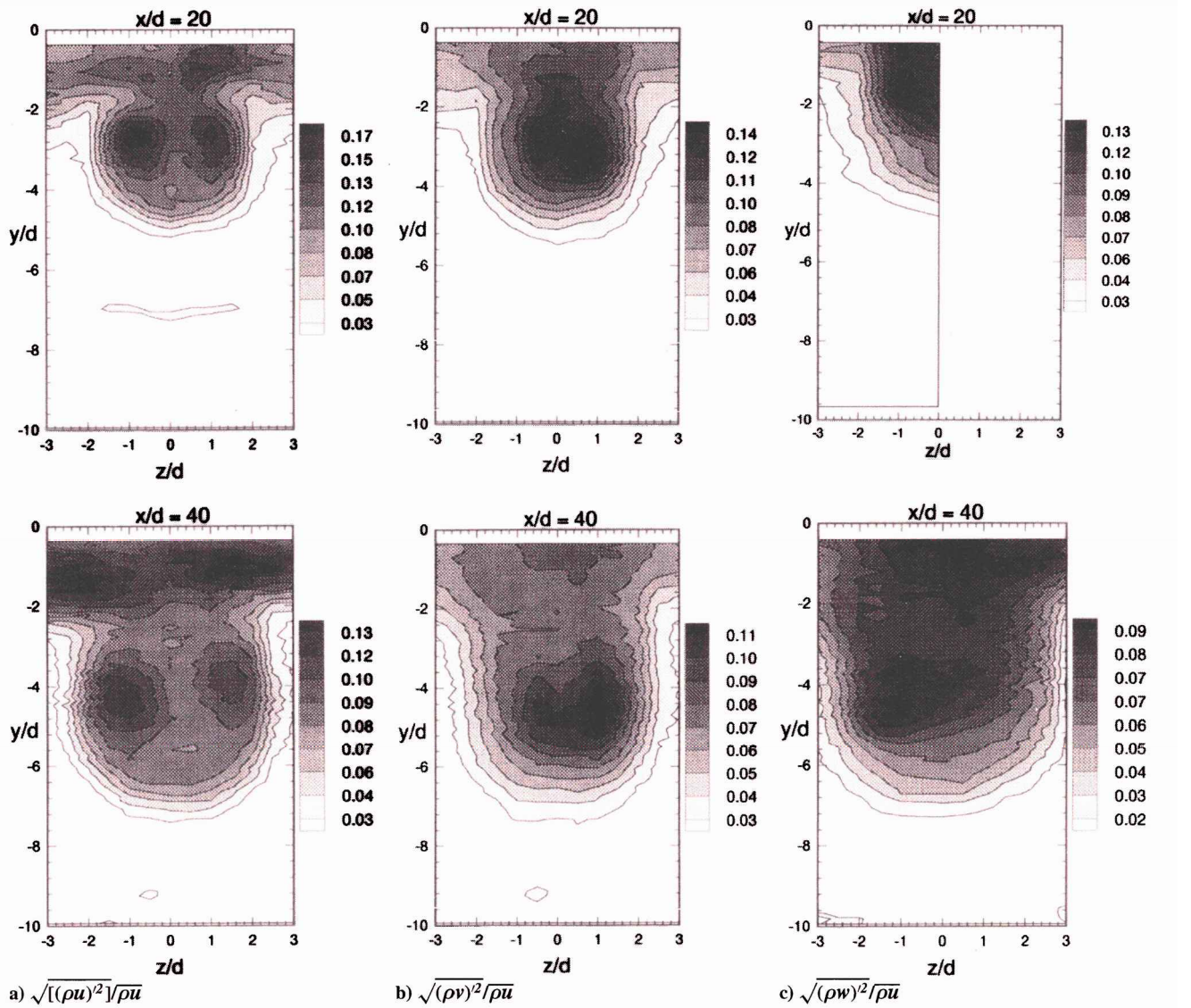

Fig. 5 Mass flux turbulence intensity contours.

only the left-hand side of the plume was mapped with the x-z probe at $x/d = 20$, with a spatial resolution of $\Delta z/d = 1.0$. Because the structure of the plume was similar between the two stations, this was not considered a limitation. The counter-rotating vortex pair is evident at both stations. Also, there appears to be evidence of a third vortex just above the main vortex on the left-hand side of the plume ($x/d = 40$, $y/d \approx 1.0$, and $z/d \approx -2.0$). Although the present data do not allow a conclusive determination, the apparent third vortex may have been the remnant of one of the horseshoe vortices, an affect of the reported unsteady wake,[15] or vorticity production due to anisotropic turbulence.

Referring to Figs. 2–4, a reasonable degree of symmetry about the z axis was observed for both stations. However, some asymmetry did exist. The asymmetry noticed here is consistent with the data of other researchers over a variety of conditions ranging from normal injection into a low-speed crossflow to low-angled injection into a hypersonic freestream. For example, the temperature contours of Kamotani and Greber[13] for the highest injection velocity case, the concentration plot for 15-deg injection into a Mach 6.0 freestream of Fuller et al.,[8] the $x/D = 8$ and 10 concentration data of Hollo et al.,[27] the $x/H = 8$ velocity vectors of Donohue et al.,[28] and the velocity vector results of Chitsomboon et al.[29] all showed evidence of an asymmetry similar to that of the present study. For the most part, the asymmetry has been attributed to upstream freestream and boundary-layer nonuniformity. The incoming flow was surveyed with the mean-flow and cross-film probes discussed earlier, and the flow was found to be uniform to within the expected measurement uncertainties. However, a number of other studies did not show the asymmetry. For example, the temperature plots for the low-injection-velocity case of Kamotani and Greber[13] and the helium concentration contours for the low-angled injection into a Mach 3.0 crossflow of Fuller et al.[8] appeared to be more symmetric. The fact that in some situations the flow remains symmetric may be interpreted as being indicative of a bifurcation point, where under certain conditions the equilibrium point shifts away from symmetry. Possible connections between this asymmetry to an interaction between the secondary motion and turbulent flow structure are discussed in the following section.

Turbulence Results

As indicated in Fig. 2b, the $x/d = 20$ station was upstream of the shock-wave interaction with the plume, and $x/d = 40$ was downstream of the interaction. The effects of expansion and compression waves on the structure of a turbulent wall boundary layer have been well established.[30–32] In addition, studies on the effects of a shock-wave interaction on the mixing[33] and turbulent flow structure[34] of high-speed free mixing layers also have been performed. Samimy et al.[34] noted that the interaction of a bow shock with a two-dimensional free mixing layer had a negligible effect on the turbulence intensity levels and the Reynolds shear stresses. Comparing the magnitudes and structure of the turbulence intensity component contour plots for $x/d = 20$ and 40 in Fig. 5, it is

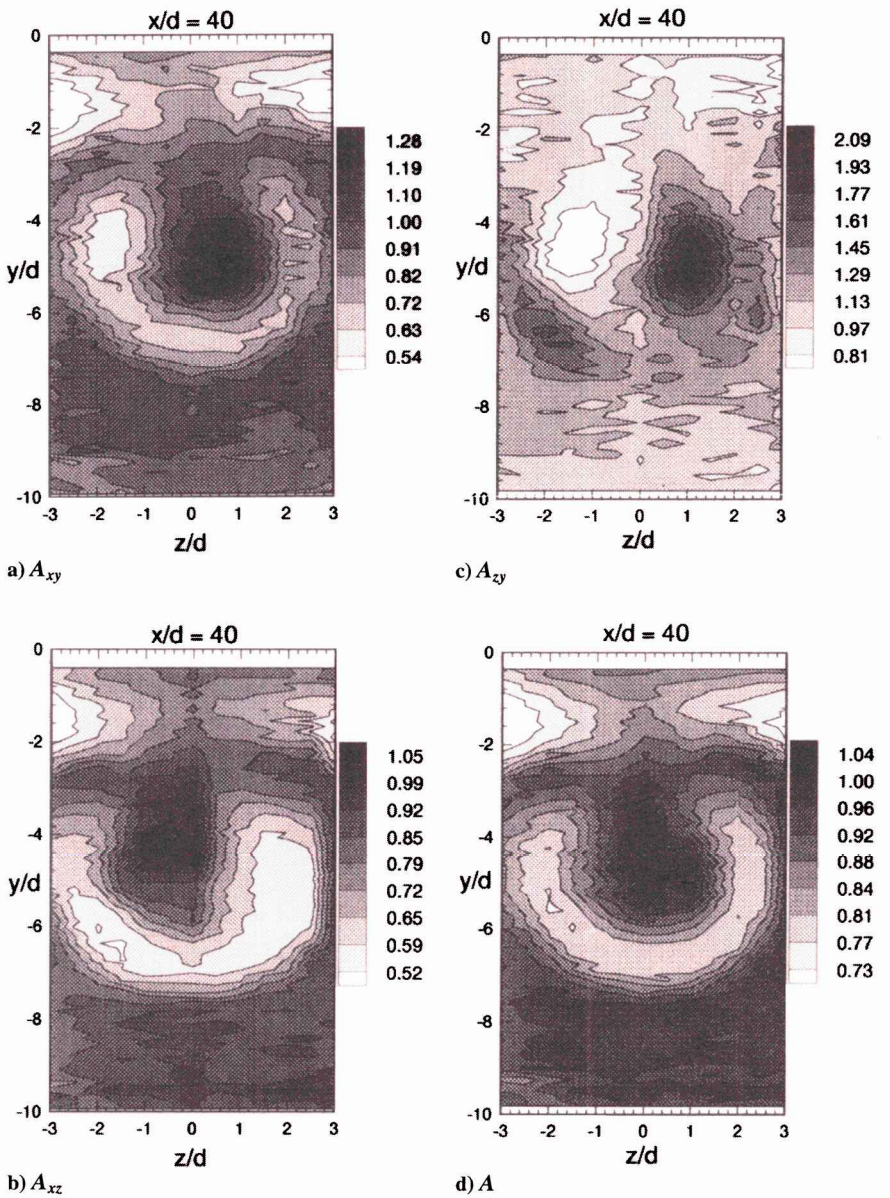

Fig. 6 Anisotropy contours ($x/d = 40$).

apparent that the results at each station were very consistent. The main difference was the increased size of the plume and the slightly lower intensity levels at the downstream location, both of which were expected. Hence, the present results were consistent with the conclusions of Samimy et al.[34]

As indicated in Fig. 5a, the axial mass flux turbulence intensity results demonstrated a strong dependence on the main vortex pair. The peak turbulence intensity levels at both stations were approximately collocated with the lower half of the vortices of the main vortex pair (see Fig. 4b). The peak values were about 17.0 and 13.0% at $x/d = 20$ and 40, respectively. Because of the reduction of the mean strain rates, it was expected that the production of the turbulence would decrease in the far field. Hence, the decrease in the turbulence intensity levels at $x/d = 40$ was expected. At both stations, the contour plots exhibited the slight asymmetry discussed in the preceding section, where the turbulence intensity levels were nominally 10% higher in the vortex region on the left side. The axial mass flux turbulence intensity magnitudes shown in Fig. 5a were in good qualitative agreement with those of the axial velocity reported in a number of low-speed studies.[13,15,16] In addition, the peak values being approximately collocated with the vortex pair also was shown by Kamotani and Greber.[13] Shown in Figs. 5b and 5c are the transverse and spanwise mass flux turbulence intensity contours. The transverse turbulence intensity plot (Fig. 5b) showed a lesser dependence on the vorticity. Interestingly, for this component, the peak value was collocated with the right side vortex. The spanwise turbulence intensity results were similar in structure to those of the transverse; however, the spanwise component peaked at a location centered in the left side vortex. Hence, the results in Figs. 5a–5c all demonstrate a strong interaction between the secondary motion and the turbulence intensity levels.

Turbulent anisotropy is an important characteristic that can affect the transport of vorticity.[35–37] Because the turbulence intensity results were found to be similar between the two stations, the anisotropy coefficients are only shown for $x/d = 40$. The four anisotropy coefficients [Eqs. (2) and (3)] are presented in Fig. 6. A_{xy} (Fig. 6a) was found to peak along the right edge of the plume center at a value of 1.28. A_{xz} (Fig. 6b) peaked along the left-hand side of the center at a value of 1.05. Around the periphery of the plume and in the boundary-layer region of the flow, the A_{xy} and A_{xz} levels of 0.5–0.7 were consistent with both low-speed boundary layer[38] and supersonic free-shear-layer[39] results. Overall, A_{xy} was higher in magnitude on the right-hand side and A_{xz} was higher on the left. As depicted in Fig. 6c, the A_{zy} coefficient also demonstrated a strong dependence on the secondary flow motion. The peak-value region within the plume on the right-hand side (centered near $z/d = 1.0$, $y/d = -4.8$) was located near the lower inner portion of the right vortex, and the minimum-value region within the plume on the

left-hand side (centered near $z/d = -1.5$, $y/d = -4.5$) was located near the upper outer part of the left vortex. Around the periphery of the plume on the lower or freestream side, A_{zy} was nominally 1.2–1.4, and on the boundary-layer side it was roughly 0.85–0.95.

The importance of A_{zy} on the vorticity field becomes apparent through an examination of the vorticity transport equation. The vorticity transport equation for compressible turbulent flow is obtained by taking the curl of the Favre-averaged compressible Navier–Stokes equations written in nonconservation form. Hence,

$$\frac{\mathrm{D}\bar{\omega}}{\mathrm{D}t} = \bar{\omega}(\nabla \cdot \tilde{V}) - (\bar{\omega} \cdot \nabla)\tilde{V} - \nabla x\left(\frac{1}{\bar{\rho}}\nabla \bar{p}\right) + \frac{1}{\bar{\rho}}\nabla x(\nabla \cdot \Pi) + \nabla\left(\frac{1}{\bar{\rho}}\right)x(\nabla \cdot \Pi) \tag{4}$$

The first three terms on the right-hand side of Eq. (4) depict the familiar compressibility and three-dimensional vortex stretching, and the baroclinic torque. The fourth term denotes the molecular diffusion and anisotropic turbulent transport, where the last term represents an anisosteric (i.e., variable density) molecular and turbulent diffusion. Because the present study was aimed at the interaction between the turbulence and the vorticity across the plume, focus was placed on the x component of the anisotropic transport term. Denoting this term as

$$\left.\frac{\mathrm{D}\omega_x}{\mathrm{D}t}\right|_A$$

it was expressed as

$$\left.\frac{\mathrm{D}\omega_x}{\mathrm{D}t}\right|_A = \frac{1}{\bar{\rho}}\left[\frac{\partial^2}{\partial y \partial z}\left(\tau^T_{zz} - \tau^T_{yy}\right) + \frac{\partial}{\partial x}\left(\frac{\partial \tau^T_{xz}}{\partial y} - \frac{\partial \tau^T_{xy}}{\partial z}\right) + \left(\frac{\partial^2}{\partial y^2} - \frac{\partial^2}{\partial z^2}\right)\tau^T_{yz}\right] \tag{5}$$

Hornung[35] demonstrated that the first term on the right-hand side of Eq. (5) was responsible for the production of the four counter-rotating vortex pairs found in straight, fully developed, rectangular duct flows. In addition, Speziale,[36] as discussed by Wilcox,[37] showed that the presence of these vortices can be predicted numerically if the anisotropic nature of the turbulence is included in the turbulence model. The standard Boussinesq model cannot predict this secondary motion.[37] To qualitatively assess the effects of the anisotropy on the vorticity, the first term in Eq. (5) was approximately evaluated using the A_{zy} data in Fig. 6c for the two nearly circular maximum and minimum anisotropy regions centered near $z/d = -1.5$, $y/d = -4.5$ and $z/d = 1.0$, $y/d = -4.8$. Plotted in Fig. 7 are lines of $1 - A_{zy}$ for these two regions [$+z/d$ and $-z/d$ correspond to the right (triangles) and left (squares) sides, respectively]. The abscissa variable r was defined as the radial coordinate measured from the center of the two symmetric regions. The four sets of data correspond to vertical (y-line) and horizontal (z-line) data profiles, which were taken along the centerlines of the two regions. The data in Fig. 6c and Fig. 7 both indicate that the two regions were reasonably symmetric, hence a polar coordinate system located at the center of each region was postulated. With this, the second derivative in the first term in Eq. (7) was estimated as $\mathrm{d}^2/\mathrm{d}r^2$. To evaluate this derivative, parabolas were fitted to the data in Fig. 7 (solid and dashed lines correspond to the y and z data sets, respectively). Thus, $\mathrm{d}^2(1 - A_{zy})/\mathrm{d}r^2 \approx 1.3 \pm 0.3$ and -0.65 ± 0.2 for the $+z/d$ and $-z/d$ anisotropic regions, respectively. The signs on the anisotropic vorticity transport are in agreement with the streamwise vorticity shown in Fig. 4 (Ref. 35). These data suggest that the vorticity production due to this anisotropy should be higher on the right-hand side of the plume. A finite difference estimate of the streamwise vorticity demonstrated that the peak vorticity on the right-hand side was about 15.0% higher than the corresponding peak on the left-hand side.[19] Recall from Fig. 5a that the axial turbulence intensity levels were about 10% higher within the left vortex as compared to those associated with the right-hand side. Hence, the higher axial vorticity damped the magnitude of the axial mass flux fluctuations.

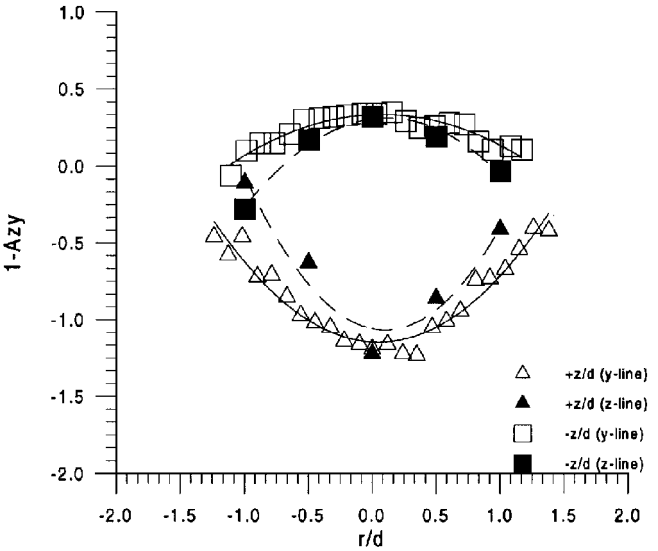

Fig. 7 Anisotropy profiles ($1 - A_{zy}$, $x/d = 40$).

These results, as well as the other gradients in A_{zy}, may have been responsible in part, via Eq. (5), for the slight plume asymmetry, or, if the asymmetry was due to a bifurcation, then the anisotropy may have influenced the preferred direction of the new equilibrium point.

Shown in Fig. 6d is the three-dimensional anisotropy parameter defined in Eq. (3). The results in Fig. 6d show that the overall magnitude of the turbulence near the center of the plume tended toward $A \approx 1.0$. Referring to Fig. 4a, it is apparent that this region within the plume corresponded to a location of relatively low mean shear-strain rate. On the other hand, it also was the location of the interaction of the two main vortices (Fig. 4b). It is expected that the highly three-dimensional strain rates in this region resulted in the nearly equal-magnitude turbulent fluctuations. Again, the anisotropy coefficients around the periphery and in the boundary-layer region were very similar to incompressible boundary-layer and two-dimensional supersonic free-shear-layer values. The relatively large mean shear-strain rates around the periphery resulted in this state of anisotropy.

Given in Fig. 8 are the x-y and x-z plane Reynolds-averaged turbulent shear stresses normalized by twice the local mean dynamic pressure, $\bar{\rho}\,\tilde{u}^2$. As indicated, the overall structure of the turbulent shear stress data was very similar between the two stations. The x-y shear stresses (Fig. 8a) were found to peak along the left side of the center of the injection plume; around the periphery of the plume, they were negative on the lower or freestream side and positive on the upper or wall side. The shear-stress signs within the boundary layer were also negative. The signs of the shear stresses around the periphery of the plume, like those within the boundary layer, did conform with conventional momentum transfer arguments.[19] Also note that the structure of the x-y turbulent shear-stress plot is very similar to that of A_{xy} and A (Figs. 6a and 6d). The peak shear-stress magnitudes along the center of the plume are also important from a turbulence modeling perspective. First, these data suggest that a standard eddy viscosity turbulence model (zero or two-equation) would not be well suited to predict the peak shear stresses along the plume center because of the relatively low magnitude of the strain rates in that region. Second, the high shear-stress levels along the plume center indicate that the turbulence in this region is highly anisotropic. It is possible that the peak shear-stress levels along the center of the plume in Fig. 8a are the result of a multimodal signal due to the inherent unsteadiness of the flow. To qualitatively investigate this possibility, the time trace from one of the cross-film sensors is given in Fig. 9. As indicated, the signal does not show any signs of being bi- or multimodal. However, if the multimodal frequencies were greater than 10 kHz, then the present experiment would not have been able to resolve them.

The x-z turbulent shear stresses (Fig. 8b, $x/d = 40$) were found to be positive over the entire flowfield and strongly dependent on the secondary motion (the peak values on both the right- and left-hand

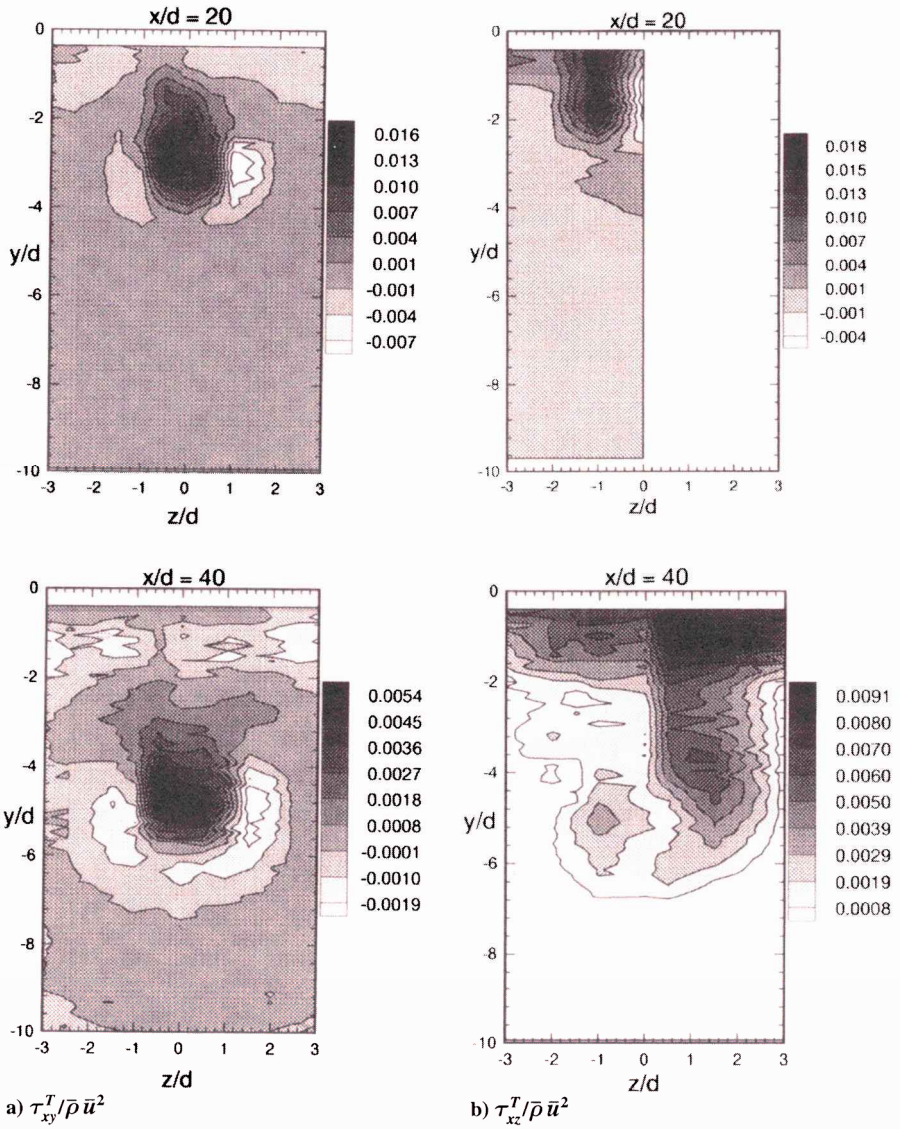

Fig. 8 Reynolds-averaged turbulent shear-stress contours.

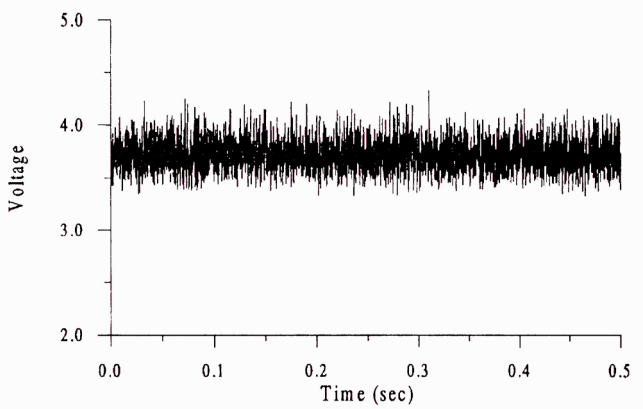

Fig. 9 Cross-film voltage signal at the plume center for $x/d = 40$; time trace for plume center ($x/d = 40, y/d = -5, z/d = 0$).

sides were approximately collocated with the counter-rotating vortex pair). If the simplistic Boussinesq turbulence model, with the secondary motion neglected, were applied, then antisymmetry about the z axis would have been expected, where the shear stresses on the left-hand side would have been negative and those on the right positive. However, as depicted in Fig. 8b ($x/d = 20$ and 40), the increased turbulent shear-stress production due to the additional strain rates associated with the secondary flow had a significant impact on the turbulent flow structure.[19] Hence, a nonlinear turbulent constitutive law is most likely required for the present flow. Thus, the nonlinear turbulent shear-stress formulation of Saffman,[40] as described by Wilcox,[37] was heuristically applied to qualitatively assess the signs of the turbulent shear stress around the plume. The x-z turbulent shear-stress formulation of Saffman[37] is given by

$$\tau_{xz}^T = \mu_T[2S_{xy} - (D/\rho k)(S_{xx}\Omega_{xz} + S_{xy}\Omega_{yz} + S_{yz}\Omega_{xy} + S_{zz}\Omega_{xz})]$$

Neglecting the axial gradients and assuming that $D \sim -1.0$ (which is roughly consistent with the models of Wilcox and Rubesin[41] and Shih[42]), the turbulent shear-stress relation reduces to

$$\tau_{xz}^T \approx \mu_T \left[\frac{\partial \bar{u}}{\partial z} + \frac{1}{2\rho k}\left(\frac{\partial \bar{u}}{\partial y} + \frac{\partial \bar{u}}{\partial z} \right) \frac{\partial \bar{v}}{\partial z} \right] \tag{6}$$

Referring to Fig. 4 to conceptually infer the signs on the mean strain rates in Eq. (6), it was deduced that the second term on the right-hand side has the potential to be positive over the entire plume [with the exception of the plume center where Eq. (6) implies a zero shear stress]. Further, the relatively high positive regions in Fig. 8b located near $z/d = -1.0$, $y/d = -5.0$ and $z/d = 1.5$, $y/d = -3.8$ corresponded to positions where both strain-rate products in the second term in Eq. (6) would produce positive shear stresses. Hence, the present measurements were reasonably consistent with the above model. The necessity of the nonlinear shear-stress formulation also would indicate that the energy transfer between the mean flow and the turbulence by way of the turbulence production would not be

symmetric across the plume and hence perhaps contributing to the asymmetry discussed earlier. The rather remarkable anisotropy between the x-y and x-z turbulent shear stresses (comparing Figs. 8a and 8b) also could have impacted the vorticity transport by way of the second term on the right-hand side of Eq. (5).

The present data suggest a strong interdependency between the secondary motion and the turbulent flow. Although not the primary focus of the research, it also was postulated that the asymmetry noticeable in the present as well as a number of other studies[8,13,27–29] was a result of this interaction. Three plausible explanations for the generation of the asymmetry have been suggested: vorticity production [Eq. (4)] due to the anisotropy, a bifurcation of the equilibrium state that was biased by the anisotropy, and an asymmetric energy transfer between the mean and turbulent flow due to the nonlinear nature of the turbulent shear-stress/strain rate relationship.

Conclusions

An experimental study, focused on examining the three-dimensional turbulent structure of an angled, overexpanded, supersonic gaseous injection into a supersonic crossflow, is presented. Schlieren photography and surface oil-flow visualization are used to provide a qualitative global picture of the present flow. Cross-film anemometry, in conjunction with conventional mean-flow probes, is used to provide both three-dimensional mean-flow and mass-weighted turbulence data. Two relatively large recirculation cells are located just downstream of the injector. In addition, the vortex pair within the plume dramatically affects the overall mean and turbulent flow structure. The axial turbulence intensity is found to have two peaks that are collocated with the vortex pair. The transverse and spanwise intensities peak on the right and left sides of the plume, respectively. The anisotropy contours also show a strong dependence on the secondary motion. In particular, the z-y coefficient has a maximum located within one vortex, and a minimum in the other. Although not a primary focus, an asymmetry across the plume was noticed. Similar asymmetries were noticed in a number of other studies over a wide range of flow conditions. Aside from possible upstream nonuniformities, three plausible explanations for the generation of the asymmetry are postulated: vorticity production due to anisotropy, a bifurcation of the equilibrium state that was biased by anisotropy, and an asymmetric energy transfer between the mean and turbulent flow due to the nonlinear nature of the turbulent shear-stress/strain rate relationship.

References

[1]Morkovin, M., Pierce, C., Jr., and Craven, C., "Interaction of a Side Jet with a Supersonic Main Stream," Univ. of Michigan, Engineering Research Bulletin 35, Ann Arbor, MI, Sept. 1952.

[2]Schetz, J., and Billig, F., "Penetration of Gaseous Jets into a Supersonic Stream," *Journal of Spacecraft and Rockets*, Vol. 3, No. 11, 1966, pp. 1658–1665.

[3]Schetz, J., Hawkins, P., and Lehman, H., "Structure of Highly Underexpanded Transverse Jets in a Supersonic Stream," *AIAA Journal*, Vol. 5, No. 5, 1967, pp. 882–885.

[4]Billig, F., Orth, R., and Lasky, M., "A Unified Analysis of Gaseous Jet Penetration," *AIAA Journal*, Vol. 9, No. 6, 1971, pp. 1048–1058.

[5]McClinton, C., "The Effects of Injection Angle on the Interaction Between Sonic Secondary Jets and a Supersonic Freestream," NASA TN-6669, Feb. 1972.

[6]Mays, R., Thomas, R., and Schetz, J., "Low Angle Injection into a Supersonic Flow," AIAA Paper 89-2461, July 1989.

[7]Schetz, J., Thomas, R., and Billig, F., "Mixing of Transverse Jets and Wall Jets in Supersonic Flow," *Separated Flows and Jets*, edited by V. V. Koslow and A. V. Dovgal, Springer–Verlag, Berlin, 1991, pp. 807–837.

[8]Fuller, E., Mays, R., Thomas, R., and Schetz, J., "Mixing Studies of Helium in Air at High Supersonic Speeds," *AIAA Journal*, Vol. 30, No. 9, 1992, pp. 2234–2243.

[9]Powlre, H., Ball, G., and East, R., "Comparison of the Interaction of Two and Three Dimensional Transverse Jets with a Hypersonic Freestream," CP-534, AGARD, 1993, pp. 20.1–20.8.

[10]Gaillard, R., Geffroy, P., Jacquin, L., and Losfeld, G., "Etude Experimentale Sur Les Interactions Entre un Jet Supersonique Chauffe Transversal et un Ecoulement Supersonique Externe," CP-534, AGARD, 1993, pp. 39.1–39.12.

[11]Schetz, J., *Injection and Mixing in Turbulent Flow*, edited by M. Summerfield, Vol. 68, Progress in Astronautics and Aeronautics, AIAA, New York, 1980, pp. 145–164.

[12]Perry, A., Kelso, R., and Lim, T., "Topological Structure of a Jet in a Cross-Flow," CP-534, AGARD, 1993, pp. 12.1–12.7.

[13]Kamotani, Y., and Greber, I., "Experiments on a Turbulent Jet in a Cross Flow," *AIAA Journal*, Vol. 10, No. 11, 1972, pp. 1425–1429.

[14]Moussa, M., Trischka, J., and Eskinazi, S., "The Near Field in the Mixing of a Round Jet with a Cross-Stream," *Journal of Fluid Mechanics*, Vol. 80, Pt. 1, 1977, pp. 49–80.

[15]Fric, T., and Roshko, A., "Vortical Structure in the Wake of a Transverse Jet," *Journal of Fluid Mechanics*, Vol. 279, Nov. 1994, pp. 1–47.

[16]Andreopoulos, J., and Rodi, W., "Experimental Investigation of Jets in a Crossflow," *Journal of Fluid Mechanics*, Vol. 138, April 1984, pp. 93–127.

[17]Bradshaw, P., "Compressible Turbulent Shear Layers," *Annual Review of Fluid Mechanics*, Vol. 9, Jan. 1977, pp. 33–54.

[18]Papomoschou, D., and Roshko, A., "The Compressible Turbulent Shear Layer: An Experimental Study," *Journal of Fluid Mechanics*, Vol. 197, Dec. 1988, pp. 453–477.

[19]McCann, G., and Bowersox, R., "Experimental Investigation of Supersonic Gaseous Injection into a Supersonic Freestream," *AIAA Journal*, Vol. 34, No. 2, 1996, pp. 317–323.

[20]Liou, W., and Shih, T., "On the Basic Second-Order Modeling of Compressible Turbulence," NASA TM 105277, Oct. 1991.

[21]Volluz, R., *Handbook of Supersonic Aerodynamics, Section 20, Wind Tunnel Instrumentation and Operation*, Vol. 6, Ordnance Aerophysics Lab., NAVORD Rept. 1488, Daingerfield, TX, 1961, pp. 49–55.

[22]Anon., *Hot-Wire/Hot-Film Anemometry Probes and Accessories*, TSI Inc., St. Paul, MN, 1989.

[23]Bowersox, R., "Thermal Anemometry," *Handbook of Fluid Dynamics and Fluids Machinery*, edited by J. Schetz and W. Fuhs, Wiley, New York, 1996, pp. 965–983.

[24]Kovasznay, L., "The Hot-Wire Anemometer in Supersonic Flow," *Journal of the Aeronautical Sciences*, Vol. 17, Sept. 1950, pp. 565–584.

[25]Spangenberg, W., "Heat-Loss Characteristics of Hot-Wire Anemometers at Various Densities in Transonic and Supersonic Flow," NACA TN 3381, May 1955.

[26]Fernando, E., and Smits, A., "A Supersonic Turbulent Boundary Layer in Adverse Pressure Gradient," *Journal of Fluid Mechanics*, Vol. 211, Feb. 1990, pp. 285–307.

[27]Hollo, D., McDaniel, J., and Hartfield, R., "Quantative Investigation of Compressible Mixing: Staged Transverse Injection," *AIAA Journal*, Vol. 32, No. 3, 1994, pp. 528–534.

[28]Donohue, J., McDaniel, J., and Hossein, H. H., "Experimental and Numerical Study of Swept Ramp Injection into a Supersonic Flowfield," *AIAA Journal*, Vol. 32, No. 9, 1994, pp. 1860–1867.

[29]Chitsomboon, T., Northam, G., Rogers, R., and Diskin, G., "CFD Prediction of the Reacting Flowfield Inside a Subscale Scramjet Combustor," AIAA Paper 88-3259, July 1988.

[30]Rose, W., and Johnson, D., "Turbulence in a Shock-Wave Boundary Layer Interaction," *AIAA Journal*, Vol. 13, No. 7, 1975, pp. 884–889.

[31]Bowersox, R., and Buter, T., "Mass-Weighted Turbulence in a Mach 2.9 Boundary Layer Including Mild Pressure Gradients," AIAA Paper 96-0659, Jan. 1996; also *AIAA Journal* (to be published).

[32]Spina, E., Smits, A., and Robinson, S., "The Physics of Supersonic Boundary Layers," *Annual Review of Fluid Mechanics*, Vol. 2, 1990, pp. 178–188.

[33]Menon, S., "Shock-Wave-Induced Mixing Enhancement in SCRAMjet Combustors," AIAA Paper 89-0104, Jan. 1989.

[34]Samimy, M., Erwin, D., and Elliot, G., "Compressibility and Shock Wave Interactions Effects on Free Shear Layers," AIAA Paper 89-2460, July 1989.

[35]Hornung, H., "Vorticity Generation and Secondary Flows," AIAA Paper 88-3751, July 1988.

[36]Speziale, G., "On the Nonlinear k-1 and k-ε Models of Turbulence," *Journal of Fluid Mechanics*, Vol. 178, May 1987, pp. 459–475.

[37]Wilcox, D., *Turbulence Modeling for CFD*, DCW Industries, Inc., La Cañada, CA, 1993.

[38]Klebanoff, P., "Characteristics of Turbulence in a Boundary Layer with Zero Pressure Gradient," NACA Rept. 1247, 1955.

[39]Bowersox, R., and Schetz, J., "Compressible Turbulence Measurements in a High-Speed High Reynolds Number Mixing Layer," *AIAA Journal*, Vol. 32, No. 4, 1994, pp. 758–764.

[40]Saffman, P., "Development of a Complete Model for the Calculation of Turbulent Shear Flows," Symposium on Turbulence and Dynamical Systems, Duke Univ., Durham, NC, April 1976.

[41]Wilcox, D., and Rubesin, M., "Progress in Turbulence Modeling for Complex Flowfields Including Effects of Compressibility," NASA TP-1517, April 1980.

[42]Shih, T. H., "Developments in Computational Modeling of Turbulent Flows," NASA CR 198458, Feb. 1996.

T. C. Lin
Associate Editor